Polarimetric SAR Applications of Sea Ice: A Review

Mohammed Shokr ⬤ , *Senior Member, IEEE*, and Mohammed Dabboor ⬤ , *Senior Member, IEEE*

Abstract—**Fully polarimetric (FP) and compact polarimetry (CP) modes are advanced technologies of synthetic aperture radar (SAR). Compared to the parameters available from traditional orthogonal backscatter coefficients, these technologies offer extra parameters, called polarimetric parameters, that fully characterizes the polarization status and the phase shift of the received backscattered signal. They include a set of ratios and correlation between co- and cross-polarization, with phase included, and another set of total backscatter power (SPAN) decomposed into power from each scattering mechanism (single-, multiple-, and double-bounce). Recent studies have demonstrated the potential of using polarimetric parameters in improving retrieval of snow and sea ice information. This review paper presents a brief background on polarimetric parameters available from the FP and CP modes and highlights their uses in applications of sea ice classification, concentration, surface features (rafting and ridging), new ice versus open water identification, thickness of thin ice, and multiyear ice surface discrimination between hummocks and melt pond. The potential of using power from the three scattering mechanisms is demonstrated in a few applications. Some information retrieved using polarimetric data cannot be retrieved using conventional SAR backscatter. This review concludes with a brief presentation on operational use of SAR polarimetric data (FP and CP) in operational ice monitoring programs.**

Index Terms—**Compact polarimetry (CP), full polarimetric synthetic aperture radar (SAR), radar scattering mechanisms, SAR applications, sea ice.**

I. INTRODUCTION

THE transmitted signal from the synthetic aperture radar (SAR) is polarized and coherent (definition of the polarization of the electromagnetic wave is presented in Appendix A). Early operational SAR systems transmitted linearly polarized signal in horizontal (H) or vertical (V) polarization and received the scattered signal in one of those polarization. Hence, the received backscatter intensity was available from a single polarization combination of transmit–received; e.g., HH, HV, or VV. Such a single-channel system was found to be of limited use in discriminating between different sea ice types or its surface features [1], [2], [3], [4]. The next milestone in SAR technology was the dual-polarization system. Here, the sensor records the received signals with two polarization combinations,

e.g., HH and HV. The extra polarization channel provides more information to resolve ambiguities between ice types. Though this system has improved the retrieval of sea ice information, it did not fully resolve the ambiguity of the ice types and surface composition. Further increase of the dimensionality of the data have been identified as a requirement in several studies (e.g., [5], [6]). This call was answered through the development of the fully polarimetric (FP) SAR system (also called quad-pol mode).

In the FP system the antenna transmits alternating pulses in the two orthogonal polarization and coherently receives the complex backscattering signals (intensity and phase) in the four polarization combinations HH, HV, VV, and VH. Therefore, the return from each pixel is represented by a 2x2 matrix, called scattering matrix. When the incident radar signal scatters off the surface, the signal may be depolarized. The cause of the depolarization is the multiple (random) bounce of the signal. Obviously, this is linked to the radar interaction with surface and volume properties of the observed scene.

Two sets of parameters can be obtained to characterize the polarimetric behavior of the scattered signal (Appendix B). One set is derived directly from elements of the scattering matrix and the other from the decomposition of two matrices (coherency and covariance) constructed from vector expressions comprised of elements of the scattering matrix. The second set includes measurements of power from each scattering mechanisms (see Section II). All polarimetric parameters can be used to enhance the classification of sea ice and retrieval of ice properties and surface features. However, some of those parameters are not independent (see Section III).

The FP system has become available onboard the Japanese L-band ALOS-1 PALSAR (2006–2011) and ALOS-2 PALSAR-2 (2014–), the Argentinian SAOCOM-1 (2018–), the German TerraSAR-X, and the accompanied TanDEM-X (2007–) though they are offered as science missions only. The Canadian RADARSAT-2 (2007–), the Japanese ALOS-2 PALSAR-2 (2014–), the Argentinian SAOCOM-1 (2018–), and the Indian RISAT-1 (2012–2017) satellites offer the CP mode as well.

While the FP SAR mode offers full polarimetric information about the radar target, its swath is too small (a few tens of kilometers) to be considered useful for sea ice operational monitoring. In order to achieve a wide swath coverage with polarimetric information, the compact polarimetric (CP) mode was proposed [7]. It can operate in a swath width ranging from few kilometers (StripMap or Spotlight) up to 500 km (ScanSAR). Therefore, it carries a potential to be the prime data source for sea ice operational monitoring. The concept and applications from this mode

are reviewed in [8]. Theoretical background about the CP mode and its polarimetric parameters are presented in Appendix C.

Just like the dual-polarization SAR, the CP mode transmits one polarization and receives backscatter in two polarizations. The difference, however, resides in the polarization of the transmitted pulses. The CP transmits circular (right or left) polarization and coherently receives backscatter from the two orthogonal polarizations. For example, the SAR antenna on the RADARSAT Constellation Mission (RCM) includes a CP mode, which transmits right circular polarized signal (R) and receives the scattered signal in the two linear orthogonal polarizations H and V; hence, it offers scattering observations with RH and RV polarization combinations. This allows construction of polarization information similar but not as complete as the information from the FP mode. Techniques for retrieving polarimetric parameters from the CP mode are presented in [9]. A few parameters have similar meaning as of the corresponding FP mode parameters.

A critical comparison between FP mode from RARADSAT-2 and simulated CP SAR is provided in [10]. The study concluded that the FP should remain the choice if high quality of cross-polarization return is the priority. Assessment of CP data from spaceborne SAR for sea ice is presented in [11]. In [12], a suite of environmental applications using simulated CP data is presented, and in [13] 23 parameters, also from simulated CP data, are evaluated for their potential applications for sea ice type discrimination.

A recent review on using the FP mode, yet without addressing the use of the scattering mechanisms, is presented in [15]. Another review that covers methods of sea ice classification from SAR data, including polarimetric data, is presented in [16]. Coverage of SAR polarimetry technology can be found in [17], [18], and [19]. This review paper includes a summary of derived parameters from the FP and CP modes, description of radar scattering mechanisms from sea ice, and examples of applications to estimate ice types, thickness, and surface features. Advantages of using these two modes, compared to traditional SAR data, are highlighted. An early review of SAR polarimetry for sea ice applications is presented in [14].

Section II introduces the three possible scattering mechanisms from sea ice and Section III introduces SAR polarimetric parameters. Section IV addresses the concept of age-based versus SAR-based ice classification. Section V demonstrates advantages of using the FP SAR in ice type classification, surface feature retrieval, and thin ice thickness estimation. Section VI summarizes studies on modelling power from scattering mechanisms, while Section VII presents a brief account on sea ice applications of CP data. Section VIII shows two possible visualization approaches of polarimetric data in operational sea ice monitoring. Finally, Section IX concludes the article.

II. SAR Scattering Mechanisms in Relation to Physics of Sea Ice

The sea ice regime usually encompasses the following major categories: open water (OW), young ice (YI), first-year ice (FYI), and multiyear ice (MYI). These categories are set by the
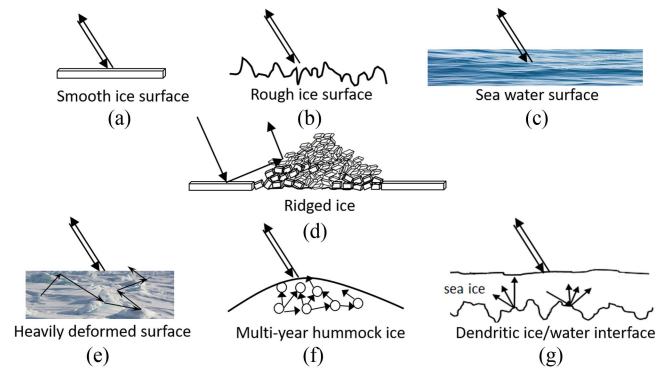

Fig. 1. Radar backscatter mechanisms from a few configurations of sea ice. (a), (b) and (c) show surfaces that trigger single-bounce scattering, (d) represents double-bounce scattering from a ridge and (e), (f), and (g) represent multiple-bounce scattering from heavily deformed surface (e), subsurface layer of MYI (f) and dendritic interface when the ice is thin enough (g).

World Meteorological Organization (WMO). Surface deformation is usually associated with YI and FYI. Radar scattering from sea ice may take the form of one or more of the following three mechanisms: single-bounce (SB) (also called surface- or odd-bounce-scattering), double-bounce (DB), and multiple-bounce (MB) (also called random- or volume-scattering). Different ice types/surfaces are associated with different mechanisms as shown in Fig. 1. SB is triggered by smooth or moderately rough surface. The DB mechanism is activated when the signal is bounced twice between two orthogonal surfaces acting as a dihedral corner. High power from the MB mechanism is observed when the incident wave undergoes many random bounces between numerous scattering elements. Further explanation of each mechanism in relation to ice types and surface features follows. Typical values of power from the different mechanisms for selected ice types/features are presented in the following section.

The following discussions applies mainly to the C-band interaction with sea ice surface but still largely true for the X- and L-band. Practically speaking, SB scattering is generated from smooth or rough but leveled (versus deformed) surfaces of YI and FYI types. This means that the total power (SPAN) is mainly composed of SB mechanism, which increases with the roughness scale. The SB is also triggered by the OW surface, regardless of its wind-driven roughness [20]. When the water surface features gravity waves with wavelength of a few centimeters under wind speed > 15 km/h, Bragg scattering is triggered and this increases the SB power but does not invoke MB mechanism [21]. The DB mechanism is likely to be generated from ridges, raised edges of sea ice floes, rafted ice or edges of icebergs or ice shelf. The MB scattering is generated from multiple (random) bounces caused by heavily deformed surface with many upturned ice blocks, a bubbly subsurface layer of the MYI hummocks, or the dendritic ice/water interface of YI. The latter situation occurs only with thin (new) ice when the radar signal penetrates the entire ice thickness. Examples are shown using color composite schemes from selected polarimetric parameters in Section VIII.

It is possible that a given ice surface may trigger more than one scattering mechanism. For example, a ridged surface may generate DB and MB scattering yet with different weights, depending on the viewing angle of the sensor with respect to the multifaceted arrangement of the ice blocks. The power from the DB scattering is always much smaller than that from the other two mechanisms, even when it is relatively high [20, Table 3]. Another example is the comparable scattering power of SB and MB mechanisms from MYI. Switching between scattering mechanisms during sea ice development is also possible. This is demonstrated when the MB scattering diminishes and gives rise to stronger SB scattering as thin ice thickens during its early growth phase. It is also demonstrated through the refreezing of the MYI surface during the fall transition season. Using Rayleigh volume scattering theory, Beaven [22] modeled the C-band scattering from MYI throughout the onset of surface freeze-up in the fall. The study concluded that the dominant scattering mechanism switched from SB to MB during that period. This was manifested in σ^o_{hv} increase by 4–12 dB. Prior to the refreezing, the flooded surface masks the subsurface bubbles that trigger volume scattering. This means that evolution of σ^o_{hv}, entropy and the ratio of MB/SB power (see Appendix B for definition) from a given ice floe can be used to mark the transition of MYI to the new freezing season.

Obviously, the scattering mechanism from the same ice depends on the wavelength and the incident angle of the radar signal with respect to the dimensions and orientation of the scattering elements. For example, the wavelength of the L-band (15–30 cm) is much larger than the characteristic dimensions of the scattering air bubbles within the MYI subsurface (a few millimeters as shown in [23], hence the MB scattering tends to be much smaller than the C-band ($\sim$ 5.4 cm wavelength). However, the scattering power from the L-band can be used to differentiate between MYI and the heavily deformed ice [24].

MYI would exhibit surface scattering at L-band, while deformed ice exhibits volume scattering. This is not the case in C-band, where both MYI and heavily deformed ice return almost equal volume scattering power.

III. SAR POLARIMETRIC PARAMETERS

A set of polarimetric parameters is available from the FP mode, and another set with similar meaning is available from the CP mode. The two sets are addressed separately in the following with more details given in Appendix B. Not all the parameters within each set are independent as indicated in this section, hence adding more parameters does not necessarily mean more retrieved information.

For the FP mode, the polarization information implied in the recorded backscatter is expressed using two sets of derived parameters. The first encompasses polarimetric ratios and coherence (PRC) between different channels, and the second, called polarimetric decomposition parameters (PDP), are derived from two second order matrices called coherency and covariance. The two sets of parameters and the matrices are presented in Appendix B. The PRCs are derived from elements of the scattering matrix, which are complex numbers combining the backscatter intensity and phase from different polarizations states. This set includes the SPAN, which is the summation of power from all polarization states. It is included in this set although it is not a ratio. The PDPs, on the other hand, are derived from decomposition of either the coherency or the covariance matrices, both are generated from elements of the scattering matrix. This set includes two subsets. The first encompasses parameters derived from purely mathematical-based decomposition approaches, such as the well-known Cloude–Pottier decomposition [25]. This is based on the eigen decomposition of the coherency matrix, and leads to three widely used parameters; the entropy (H), anisotropy (A) and alpha-angle (α). These are proxy indicators of the scattering mechanisms. The second subset encompasses a model-based decomposition approach, such as the Yamaguchi decomposition [26], which uses the covariance matrix. Herein, another three parameters are derived. They are direct measurements of power associated with the three scattering mechanisms; SB, DB, and MB; denoted P_s, P_d, and P_v, respectively. Yamaguchi decomposition has an extra parameter linked to the helix scattering, which is usually observed in urban area. This parameter is ignored in sea ice studies.

A few studies compiled databases of selected PRCs for sea ice [27], [28], [29], [30] and even fewer studies compiled data from PDPs [31], [32], [20]. In general, those datasets were acquired on opportunity bases using spaceborne polarimetric SAR or ground-based scatterometer systems. A comprehensive database that encompasses values from different ice types with different surface features is yet to be established. The challenge in this task is the need for fully characterization of environmental and ice conditions from a wide range of snow-covered sea ice during radar data acquisition. Obviously, *in situ* field measurements are required for this task. Given the intention to accelerate the operational use of the CP SAR mode, it is hoped that such a comprehensive database will be developed in the next few years.

The first and most comprehensive dataset of 20 selected PRC and PDP parameters (derived from Cloude-Pottier, Yamaguchi, and Touzi decompositions presented in Appendix B) from 3 sea ice types: smooth FYI (SFYI), rough FYI (RFYI), and deformed FYI (DFYI) in addition to wind-roughened open water were compiled in [28]. Data were obtained from the FP mode on RADARSAT-2, acquired over Parry Peninsula in Franklin Bay, Western Arctic in April 2008. The study related some of those parameters to physical characteristics of the surface through field measurements and observations. Smaller databases were compiled in [33] and [34]. However, none of those studies examined correlations between PRC parameters, except for the anticipated correlation between σ^o_{hh} and σ^o_{vv}. Some indications of correlation between specific parameters for specific ice types are apparent in the data in [30].

Values of PDPs from different ice types and water surface are presented in [20] using 31 scenes of RADARSAT-2 FP fine mode over Resolute Bay in the Canadian Arctic during the period of September–December 2017. The study pointed out a few rules that link the scattering mechanisms to sea ice and water surfaces identification. For example, thin ice of a few centimeters thickness instigates high MB scattering,

which diminishes gradually as ice thickens in favor of higher SB scattering. Deformed ice surface triggers high backscatter intensity composing of SB, MB, and perhaps relatively high DB in the presence of large deformed surface (upturned ice blocks). Different scattering mechanisms are revealed from hummock and melt pond surfaces (more on their physical characteristics can be found in [35]). Hence, these two surfaces can be identified based on examination of the power from the three scattering mechanisms (see Section V-A). In addition, the ratio P_v/P_s can be used to discriminate MYI from FYI and identify new ice [20]. When this ratio is calculated in dB, it is simply the arithmetic difference of P_v minus P_s in dB.

Very few studies examined correlation between FP parameters for sea ice application (e.g., [36]). Only PCR parameters may show dependence or correlation within this set or with a few parameters from the PDP set. On the other hand, all parameters within the PDP set are independent as each parameter represent different scattering process. For example, H and α (see Appendix B) are independent because the former gives information about the number of the scattering mechanisms, while the latter gives information about the type of the mechanisms. Obviously, the three scattering power parameters p_s, p_v, and p_d are also independent. However, their values may not uniquely identify the ice or surface types. For example, P_v is equally high from new ice, DFYI, and MYI. Recent ice history and climatic data should be incorporated in the analysis to resolve this ambiguity.

As for the CP mode parameters, a database was compiled, for the first time, for selected sea ice types in [37]. Twenty-six parameters were simulated from RADARSAT-2 FP mode to represent nine ice types covering all seasons over the Arctic region. A comprehensive table showing regression models of each parameter as a function of incidence angle for each ice type is also presented in [37]. A unique feature of this study is the development of four groups of correlated parameters using Spearman's rank correlation and relating the groups to the scattering pattern from sea ice and water. This grouping was used in [11] and [38]. This approach should be pursued when testing a large set of polarimetric parameters since a few CP parameters are possibly correlated and related to certain surface or volume conditions [24], [39].

It would be appropriate to conclude this section with a note on multifrequency FP airborne SAR systems, which have been used in scientific sea ice research. The earliest system was NASA's airborne AIRSAR (P-, L-, and C-band) [40]. It operated between 1988 and 2004. Another system, operated by the Canada Center for Remote Sensing in the late 1980s onboard Convair-580 aircraft, was used in a limited qualitative manner to identify ice types during research field expeditions. The Danish dual-frequency (L- and C-band) FP system (EMISAR), operated in 1990s and data were used in a limited number of studies for sea ice classification [41]. The German DLR F-SAR system operates in X-, C-, S-, and L-band. It was used to characterize sea ice in the Davis Strait off the coast of Baffin Island [42].

Between the above-mentioned multifrequency FP systems, AIRSAR was the most frequently used so far for ice classification (see Section V). Selected PRC parameters; namely SPAN, copolarization and cross-polarization ratios, phase difference, and copolarization correlation coefficient were tested in [14]. So far, no multifrequency polarimetric SAR is available from a single satellite platform. A few studies used coincident multifrequency data from different SAR platforms for ice classification as presented in the next section. The potential for using multifrequency polarimetric data from multiplatform is promising as more future polarimetric SAR systems with different frequencies are scheduled for launch. Examples include the Japanese L-band ALOS-4 (scheduled for launch by the end of 2023), NASA-ISRO dual frequency (L- and S-band) NISAR system (scheduled for launch in 2023), and ESA's L-band ROSE system (scheduled for launch in 2028).

IV. AGE-BASED VERSUS SAR-BASED SEA ICE CLASSIFICATION

Traditional applications of SAR data for sea ice use backscatter coefficient to map ice types according to "stage of development" (SOD) categories set by WMO. [43]. These are ice-age-based categories, which usually imply ice thickness. This categorization, however, is problematic for SAR data because the received backscatter is primarily sensitive to surface roughness, subsurface composition of the snow and ice cover, and dielectric constant, which is affected by ice salinity, temperature, wetness, and snow metamorphism. None of those parameters is uniquely related to the ice age or thickness. For this reason, SAR backscatter intensity data can only be used as proxy indicators of ice categories based on SOD. The most successful use of SAR backscatter has been demonstrated in identifying MYI, which triggers higher backscatter compared to other SOD-based ice types because of its bubbly subsurface layer. However, the backscatter can be equally high from deformed ice. Attempts to resolve this ambiguity in identifying deformed ice are presented in [15] and [44]. The power from scattering mechanism can also be used to resolve this ambiguity as demonstrated in Section V.

Using SAR to its full potential for sea ice classification and surface feature identification requires refrainment from forcing the data to identify the unwarranted age-based discrimination such as open water versus new ice, new versus young ice, thin versus think FYI, grey versus grey-white ice, and second-year versus multi-year ice. The overlap of the backscatter between different ice types (and open water) stimulates the use of contextual information and ancillary data of weather, climate, recent ice history, and other remote sensing observations to support the image analysis. When this information is incorporated in a knowledge-based system to automate the classification [45] the operational use of the system lacked the required robustness.

A better use of SAR data would be achieved by switching from the SOD-based ice categorization to a SAR-based ice categorization. The latter includes, for example, level versus rough or deformed ice surface, annual versus perennial ice, and bare versus snow-covered ice when snow metamorphoses. SAR-based categorization has not been thoroughly explored using the traditional backscatter coefficient data. Given the extra observations available from the FP and CP SAR modes, more effort should be dedicated to develop a SAR-based categorization.

This will particularly benefit from the scattering mechanisms from ice types and surface features.

When power from scattering mechanism is used, more relevant SAR-based categories can be identified, which include the following:

1) new ice versus open water;
2) thin new ice (nilas) within the young ice category;
3) hummock versus melt pond ice of MYI;
4) deformed (ridged) versus levelled or rough ice surface.

Examples that highlight those categories are included in the following section. This endeavor should receive more attention in future studies, given the increasing availability of spaceborne CP data and the plans of their use in the operational ice monitoring programs.

V. RETRIEVAL OF SEA ICE PARAMETERS AND SURFACE FEATURES

A. Sea Ice Classification

Early interest in SAR data for sea ice grew in the 1990s. It was motivated by the need to develop a computer-assisted age-based sea ice classification scheme to support the operational ice monitoring. The earliest investigation of FP data for ice classification was presented in [14] using NASA's AIRSAR data. The study showed clusters of OW, MYI and a few subcategories of FYI data in a 2D feature space comprising the co-pol ratio ($R_{hh/vv}$) and the standard deviation of the difference between σ_{hh}^o and σ_{vv}^o returns. Only a potential for ice type classification from that set was shown but the authors hinted to the possibility of identifying thin ice using the FP mode, which was verified in later studies. They also emphasized the importance of the embedded phase information in the FP data, which appears in the correlation between backscatter from different polarizations (part of the PRC parameter set). Another study classified FYI and MYI using a neural network technique applied to the same AIRSAR data is presented in [46]

As SAR FP data became more available later from airborne and spaceborne platforms, several studies explored the potential of using the data in sea ice classification while applying different classification approaches. The study in [47] investigated SAR FP capability, obtained from the C-band onboard the space shuttle SIR-C, in discriminating ice types using PDPs and the complex Wishart classifier in an unsupervised classification scheme. While no conclusive results were presented, the study confirmed the advantage of increasing the amount of information in initializing the minimum distance classification, especially by adding σ_{hh}^o, $\sigma_{hh}^o/\sigma_{vv}^o$ and the anisotropy (A). Another study [48] tested several applications of an unsupervised segmentation based on the Wishart distribution of FP airborne C- and L-band. Results confirmed the domination of surface scattering from all seasonal ice types, yet with presence of volume scattering component. No statistical details of their ratio in relation to the ice cover was presented. The study also confirmed, for the first time, that the dihedral scattering (DB) rarely dominates the received backscatter. The initialization of the segmentation method with a scattering power proved to be an efficient step that improved the results. That was also a first hint to the potential use

the scattering power available through the PDPs. In [49], Marino et al. tried to separate different ice types in multidimensional spaces using PRC parameters and the Wishart classifier using the covariance matrix derived from FP data. In [50] Brekke et al. used the polarization ratio with dielectric constant modeling from a multifrequency polarimetric data (X-, C-, and L-band) to detect oil spill in thin ice. While they found that the FP data (with phase information) useful for discriminating the two surfaces, the dual-polarization data (without the phase information) was not useful for this purpose.

Polarimetric SAR from two airborne sensors, the Danish EMISAR and NASA's AIRSAR, acquired over the Greenland Sea, Baltic Sea, and Beaufort Sea, were used in a hierarchical sea ice classification scheme [15]. The use of the polarimetric phase information was found to improve the classification only in the case of thin ice types but not necessary for ice above 30 cm thickness. In [51], Dabboor and Shokr used RADARSAT-2 FP data in the supervised Wishart classifier to classify OW, smooth, rough, and deformed FYI in Franklin Bay, Canadian western Arctic. They used the coherency matrix at each pixel (spatial context information) with a new Bayes risk function that can be minimized to obtain a Likelihood Ratio (LR). The study showed the improved classification accuracy when LR is incorporated into the classifier. In [52], six PRCs, obtained from RADARSAT-2 FP data north of Svalbard are used in an automated segmentation and classification algorithm. The study used various statistical distance measures to automatically assign classes to the statistically nearest reference class. Classification accuracy was found to depend on the incidence angle.

In [53], Ressel et al. examined the performance of a neural network classifier based on polarimetric features derived from TerraSAR-X data. Data from YI, smooth FYI, rough FYI and OW were obtained north of Svalbard. The study found the SPAN and other parameters based on the covariance matrix to be more useful than eigenvalue decomposition-based parameters. Feature space composed of PDPs to classify ice types in the central Greenland Sea from the ALOS PALSAR FP data are used in [54]. The study concluded that the target decomposition based on scattering model can provide better capability to identify water and sea ice, compared to eigenvalue H/α/A decomposition. PDPs based on covariance matrix and coherency matrix decomposition were ingested into a trained neural network classifier and found to be more efficient [55]. Ice/water classification was achieved at 100% accuracy and sea ice type classification was achieved at less accuracy. The analysis reveals similar results from X-band TerraSAR-X/TanDEM-X and C-band RADARSAT-2 data, and slightly different results from the L-band ALOS-2 data.

Evaluation of potential application of FP SAR from C-band RADARSAT-2 and L-band ALOS-2 imagery for monitoring and classifying sea ice during dry winter conditions is presented in [24]. Twelve polarimetric parameters were derived and their capabilities of discrimination between FYI and Old Ice (OI) was examined. The Random Forest classification algorithm was used. Fig. 2 shows the classification results overlaid on the regional ice chart of 27 April 2015 over Victoria Strait in the Canadian Arctic Archipelago, produced by the Canadian Ice Service (CIS). The noticeable observation is the merge of OI floes in
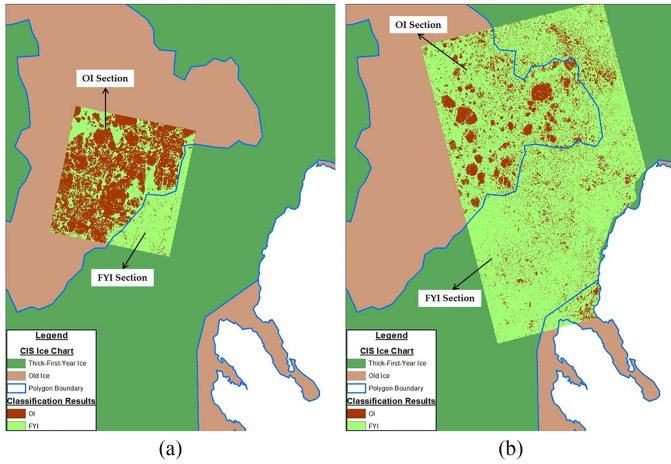
(a)   (b)

Fig. 2. Classification results of FYI and Old ice overlaid on sea ice chart from the CIS for April 29, 2015 over Victoria strait in the Canadian Arctic Archipelago (CAA). Classification was based on SAR data from FP mode using (a) RADARSAT-2 and (b) ALOS-2 SAR [24].

Fig. 3. Multiyear ice floe in the *SPAN* image (top-left panel), acquired by RADARSAT-2 FP mode on November 20, 2017 in resolute passage, central arctic. The red box shows a frozen melt pond ice in dark tone surrounded by a hummock surface in bright tone. Images of different scattering parameters of the area marked by the red box are shown. Note the contrast between melt pond (at the core) and surrounding hummock surfaces in each parameter. Note also the high DB power around the hummock [20].

the RADARSAT-2 data and their separation in the ALOS-2. This occurs in an area defined as 100% OI coverage in the ice chart. In general ice type classification using the fine-resolution SAR data (regardless of the SAR acquisition mode) reveals unprecedented details about individual or conglomerated ice floes that cannot otherwise be identified in the conservative estimates revealed in operational ice charts. The L-band data was able to identify MYI floes and separate them from Second Year Ice (SYI). The same study in [24] showed that the data fusion of FP C-band and L-band could characterize FYI, SYI, and MYI.

The performance of FP data from the Chinese GF-3 satellite was investigated in [56] for classification of three types: ice floes (regardless of the type), open water, and brash ice in the Arctic Ocean during late spring and summer. PRC parameters were used in a classification scheme, which employs a residual convolutional network called MSI-ResNet. More details in discriminating individual sea ice floes are revealed from using PRC data than the conventional SAR data (comparison was performed using coincident Sentinel-1A Extra Wide (EW) data). To the best knowledge of the authors of the present review, the study in [56] is the only one that compared the performance of sea ice classification using FP and coincident conventional SAR data. More studies should use this methodology to further highlight the SAR-based classification approach.

An attempt to explore the potential of using the relative power from radar scattering mechanism, derived directly from Yamaguchi decomposition of the covariance matrix (see Appendix B) is presented in [20]. The study shows, for the first time, the ability of using the PDPs (including the relative weight of the power from the SB, MB, and DB mechanisms) in discriminating between the two surfaces of MYI: hummocks and melt pond. Fig. 3 shows a MYI floe as appears in the seven parameters identified in the panels. The content of the red box in top-left panel (SPAN) is enlarged in the rest of the panels. The microlook of the contents reveals a large area of low SPAN in the middle of the floe, which is interpreted as frozen melt pond, surrounded
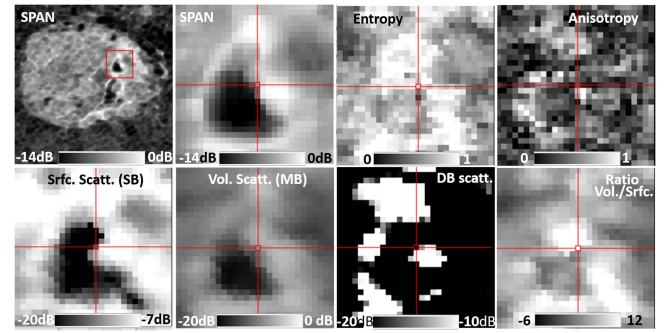
by high backscatter around its boundary, interpreted as hummock surface. This is an acceptable interpretation because the subsurface of a hummock and melt pond ice are bubbly and nearly-bubble-free, which trigger high and low backscatter, respectively. The PDP parameters: entropy, P_s, P_v, and (P_s/P_v) from hummock ice are higher than those from melt pond ice. Those parameters can be used to discriminate between the two surfaces. Another striking observation from Fig. 3 is the apparent high DB from the hummock area around the melt pond ice (though its absolute values still low, around -19 dB). This is conceivable as hummock and melt pond usually coexist next to each other, possibly making semi-dihedral configuration.

Most of the studies that investigate polarimetric SAR data for sea ice information retrieval use PRC parameters from FP mode. A few studies used PDP parameters and even fewer studies used the scattering mechanism power subset (part of the PDP). This subset is expected to be further examined as spaceborne CP data become more available to users.

Sea ice classification using multifrequency polarimetric SAR onboard AIRSAR is presented in [57]. The authors used the SPAN from the AIRSAR C-, L- and P-band to discriminate between NI, smooth FYI, ridged FYI and MYI. Wishart classifier for unsupervised classification was used. False color image of the SPAN from the 3 frequencies was presented and demonstrated excellent separation between the ice types and surface feature. Surface and volume scattering power images of the Freeman-Durden decomposition using C-, L-and P-band data are presented in [58]. The three frequencies are equally good for discriminating new ice (NI), FYI and MYI. In [24] a new potential for discriminating SYI from MYI is shown by combining C- and L-band SAR (from polarimetric RADARSAT-2 and ALOS-2, respectively) in dry ice winter conditions.

B. Ice Surface Features

Sea ice surface features include smooth, rough, deformed, and melt pond ice cover. While the first three types need SAR data, melt ponds can be identified better at fine resolution accuracy
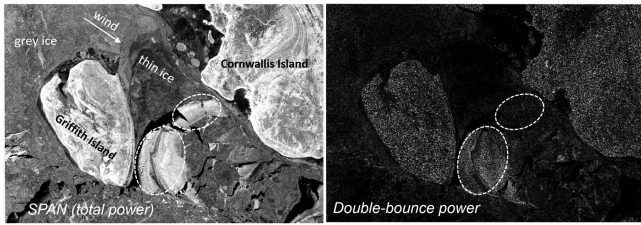
Fig. 4. Total backscatter power (*SPAN*) image of an area in lancaster sound, Canadian arctic acquired from RADARSAT-2 quad-pol acquired on 14 November 2017 (left panel), showing a large area of rafted ice marked by the dotted ellipses (identified in the ice chart by CIS). The double-bounce scattering power image (p_d) is presented in the right panel and shows high p_d from one rafted piece (RADARSAT2 is © of MDA and the image is courtesy of the CIS).
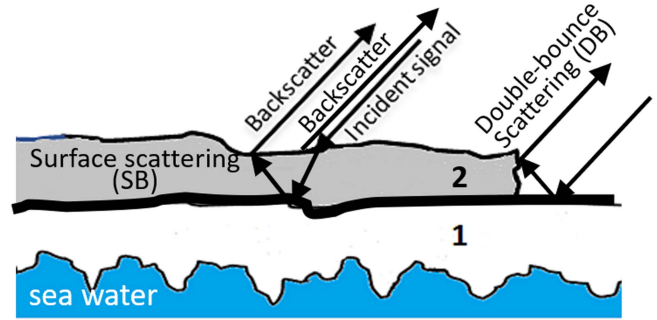

Fig. 5. Radar scattering mechanism from rafted ice. The top piece (2) has lost its dendritic configuration at its bottom surface as it slides on top of the bottom (thicker) piece (1). The interface between the 2 pieces is filled with highly saline water or ice. Two scattering mechanisms are shown, SB scattering off top and bottom surfaces of piece (2), and DB scattering off the dihedral shape of the raised edge of piece (2).

using optical remote sensing or just airborne cameras. Many methods have been developed to discriminate between ice surface roughness scales using single and dual-channel SAR [59], [60], [61], [62]. On the other hand, a few studies explored the potential of using FP SAR for this purpose. A brief account of the use of FP data is presented here but it suffices to mention that this work is still in progress with no conclusive results so far.

Drawing on the use of X- and L-band SAR polarimetry and interferometry, the study in [63] developed an approach for roughness-based ice classification (smooth, rough, and deformed) when associated with dynamic deformation of FYI. The interesting part of this study was using the conventional H/α parameter space from the eigenvector decomposition of the coherency matrix (see Appendix B). Surprisingly, the study found that smooth ice falls into the sector of dominant MB (volume) scattering while some ridged areas demonstrated strong SB (surface) scattering. This unusual result suggested that H/α feature space is not suited for in-depth analysis of ice surface roughness. Wishart classification had to be applied to arrive at optimal segmentation through maximum likelihood classification. The study in [64] explored the surface roughness signatures of the snow-covered first-year sea ice during Arctic summer in X-band dual-polarimetric SAR in terms of the root mean square (RMS) height (dual-polarimetric here means the inclusion of the phase measurement). TerraSAR-X and TanDEM-X were used for this purpose. A total of five PRCs, including copolarization ratio, copolarization phase difference, and copolarization correlation coefficients were used. Those parameters showed a statistically significant correlation with the RMS height of the sea ice (i.e., mesoscale surface roughness) but only at mid-incidence angle. σ_{hh}^o and the copolarization phase difference were found to be most sensitive to the macroscale RMS height of the sea ice.

One form of surface deformation, which is commonly observed in young ice (< 30 cm thick), is rafting. If two thin ice sheets/floes collide, the thinner sheet may be pushed up on top of the thicker one. This is how rafting forms and it is visually identified in nature. It may also be identified in SAR images by its high backscatter as shown by the marked dotted ellipses in Fig. 4. The figure shows also the p_d image with its relatively high value (-17 to -20 dB) of the rafted area. The high SPAN and relatively high p_d associated with the rafted ice are explained

as follows. The explanation demonstrates how the power from each scattering mechanism (as opposed to the total scattering power) can be useful in identifying this ice type.

The ice rafting process is shown in the sketch in Fig. 5. One piece overrides the other and the content of the layer between the two pieces is most crucial for explanation of radar scattering mechanisms. The top piece (2) has originally a dendritic surface at its bottom but the dendrites are removed when the piece slides over piece (1). This leaves the layer between the two pieces filled with sea water or highly saline ice upon freezing. In either case, it constitutes a strong dielectric mismatch. In [65], the study presented a one-dimensional thermal consolidation model for rafted ice. It proposes that rafting is composed of two or three ice layers separated by thin layers of ocean water, which freeze within 15 h. Based on this configuration, the SB scattering mechanism component becomes active not only at the surface of the top piece but also at the highly scattering layer of the dielectric mismatch at the interface between the two ice pieces. That is the reason for the observed high backscatter from rafted ice. Moreover, a DB component may be triggered by the raised edges of the rafted pieces (see Fig. 5).

Another ice surface features that can benefit from the polarimetric SAR data is the melt pond. The progress of SAR from conventional single-polarization to FP has advanced melt pond identification methodologies [66], [67], [68], [69], [70], [71]. In [66], Kim et al. used FP radar scatterometer data from test sites representing marginal ice zones in the Canadian Arctic. The copolarization ratio [this is a polarimetric parameter since it involves the phase measurement as shown in (B-3)] was shown to identify melt pond formation and fraction. Cross-polarization backscatter intensity shows potential for discriminating the onset and duration of freeze up events. The retrieval of MP fraction on MYI surface in Chukchi Sea has been investigated in [69] using polarimetric X-band SAR. The study used a rule-based machine learning approach to identify key polarimetric parameters for melt pond detection. A total of eight polarimetric parameters: σ_{hh}^o, σ_{vv}^o, copolarization ratio, copolarization phase difference, copolarization correlation coefficient, alpha angle, entropy, and anisotropy were examined. However, discrimination between

melt pond and open water was not accurate. The study in [69] found the most promising parameters to be σ_{hh}^o, its standard deviation, the average of the copolarization phase difference and the alpha angle are most promising parameters. The study in [70] retrieved melt pond fraction using polarimetric features from X-band SAR. Copolarization ratio was found to be the most promising SAR feature but the retrieval depends on wind speed and radar incidence angle. Using FP SAR mode from RADARSAT-2, the use of copolarization parameter for melt pond retrieval was confirmed in [71]. The authors also showed the benefit of using the CP mode for melt pond fraction estimate. Good correlation was found between melt pond fraction and a few PRC parameters in [67]. The strength of the regression model was improved when SAR parameters were combined with texture parameters. It is important to note that all the above-mentioned studies use PRCs, not PDPs. This is understandable because the water surface engenders SB scattering mechanism only, regardless of the surface roughness or whether it is of melt pond, open lead, or open sea (see Section II).

C. Sea Ice Thickness

Sea ice thickness retrieval from SAR is based on the premise of rapid desalination from within the ice cover during the early growth phase. This causes monotonic increase in backscatter as ice grows [72]. The increase continues until the salinity stabilizes when the thickness reaches ∼30 cm. Copolarization ratio from dual frequency (X- and L-band) FP airborne SAR system was used in [73] to estimate ice thickness. The study found that this ratio was not sensitive to small scale roughness and decreased linearly with ice thickness up to 120 cm thick. However, the relationship over such a wide range of ice thickness was not confirmed in later studies and the method did not find wide applications. In [74] the method was improved by the empirical integral-equation method surface scattering model. The study in [75] revealed a correlation between polarization ratio (co- or cross-polarization) and ice thickness (whether leveled of deformed). It asserted that this ratio could discriminate between FYI and MYI because of the different scattering mechanisms. The study used numerical model simulation of scattering mechanisms to explain their correlations with ice thickness. In another study [76], the phase difference between HH- and VV-polarization was found to enhance classification of thin ice. In [77] Johansson et al. used FP data from X-, C-, and L-band satellite SAR systems to study the effect of the growing properties of thin ice on backscatter coefficient and copolarization ratio but without quantitatively relating the thickness to those parameters.

The potential use of PDPs for thin ice thickness was examined in [32] using the FP mode of RADARSAT-2. The authors developed nonlinear regression equations between thin sea ice thickness (calculated using an empirical model) on one hand, and individual PDPs; namely, SPAN, H, α, p_v, and polarization ratio on the other hand. The premises of this relation is the possible high MB scattering power triggered by the interaction of the penetrated radar signal with dendritic surface of the bottom ice interface, while this interaction fades gradually as the ice

thickens up to 10–15 cm and the radar penetration falls short of reaching the interface (see Fig. 2). The study in [39] aimed at exploring the potential interpretation of the four parameters of Touzi decomposition: α_s, ϕ_s, ψ, and τ_m (see Appendix B) in relation to modeled thermodynamically grown lake and sea ice. For lake ice, the scattering type magnitude α_s reveals a significant decrease during the initial growth when the ice is thin (∼ 13.5 cm). For sea ice, α_s reveals also a linear decreasing trend during the early ice growth phase (∼ 30 cm), which is associated with a drop of bulk salinity. The study found also an increasing trend of the ψ parameter within the first 20–23 cm for sea ice before dropping back to zero.

VI. MODELING SCATTERING MECHANISM POWER FROM SEA ICE

A pioneer study that developed a composite model for polarimetric backscattering signature of sea ice is presented in [78]. The model incorporates typical physical, structural, and electromagnetic properties of sea ice and their interrelating processes. It is used to interpret polarimetric signature of various ice types. Refrozen ice in leads was modeled with a brine skim layer. Snow-covered FYI was modeled considering scattering from snow with spheroidal ice crystals and ellipsoidal brine inclusions. Scattering from MYI accounted for hummocks with surface tilting effects and composite rough interface.

The work in [79] examined the utility of a three-component scattering model to discriminate between snow-covered smooth, rough, and deformed FYI. At 29° incidence angle, the model shows the dominance of surface scattering from smooth, tough, and deformed FYI (77.3%, 66.0%, and 61.1%, respectively). Volume scattering is found to be the second dominant mechanism for the same three types (19.1%, 32.2%, and 37.4%, respectively). It is generated from snow layers with enlarged snow grains. The double-bounce scattering contribution is much lower for all three types. Relative fractions of the power from the three scattering mechanisms decreases with increasing incidence angle and surface roughness. In [80] Zhang et al. used a three-component scattering model to decompose polarimetric SAR data of sea ice. Backscatter was modeled as incoherent summation of SB, MB, and DB scattering mechanisms plus residual component (a measure of scattering contributions not accounted for). The model was used to validate scattering mechanism power from FYI in the Bohai Sea, obtained from RADARSAT-2 FP mode. Results show that the dominant scattering mechanism is SB, which means that the backscatter is mainly engendered by smooth or moderately rough surface. The study also showed that volume scattering increased with increasing penetration depth and increasing brine cells. In [58], Scheuchl et al. discussed the scattering decomposition models of polarimetric SAR sea ice data and their role in the ice classification. The scattering models were found to be useful in interpreting the sea ice classes. Surface scattering was found to be the dominant for seasonal ice types.

VII. SAR COMPACT POLARIMETRY

Applications of CP data for sea ice monitoring are on the rise since this mode has been incorporated in the Canadian

RCM, which has been declared operational on December 19, 2019. Even before that date, several studies were launched using simulated data from RADARSAT-2 FP mode to demonstrate the operational advantages of this mode for sea ice. Most of the studies address the potential use of CP data for sea ice classification with only a few studies addressed retrieval of sea ice thickness. Once again, most of those studies were based on simulated CP SAR data [36], [37], [81] and only a few studies used real CP SAR imagery from RISAT-1 [11], [38].

A first attempt to explore the best CP parameters for ice classification has been presented in [13]. Dabboor and Geldsetzer applied a maximum likelihood classification approach using different combinations of CP parameters and determined the best combination based on the classification error. A few CP parameters, particularly the circular cross-polarization ratio and volume scattering of the $m-\chi$ and $m-\delta$ decompositions outperformed the conventional linear polarization parameters. Simulated CP data from RADARSAT-2 were used in [81] within a scheme of support vector machine (SVM) to classify ice types. The study concluded that best classification results were obtained using all derived CP features for the SVM labeling. In [82], Zhang et al. assessed simulated CP data and recommended a few parameters for sea ice detection and classification. Response from 22 CP parameters to modeled thin sea ice thickness under thermodynamic growth were examined in [26]. Only 14 CP parameters were visually identified to be sensitive to ice thickness. The absolute correlation of the identified 14 parameters was found to be > 0.75. The $m-\chi$ decomposition parameters (see Table I) achieved the highest absolute correlation ($\sim$ 0.95). The study provided indications that the orthogonal backscattering coefficients σ_{hh}^o, σ_{vv}^o, and σ_{hv}^o might be sufficient for estimation of thin sea ice thickness.

In [11], the study evaluated, for the first time, the potential of spaceborne CP data in retrieval of sea ice parameters in Fram Strait and northeast Greenland. Espeseth et al. used 13 CP features obtained from the SAR onboard Radar Imaging Satellite (RISAT-1) in September 2015 and the results indicated a similar separability between the sea ice types using simulated CP data from RADARSAT-2. The best features that separate FYI, MYI, and open water are the intensity coefficients from the right-hand circular transmit, the linear horizontal receive channel and the right-hand circular on both the transmit and the receive channel. RISAT-1 was declared nonoperational in March 2017 after 5 years in orbit. RISAT-1A, a follow-up on RISAT-1, was launched in February 2022 but no sea ice applications of the data have been published yet.

The study in [83] presented an interesting attempt to retrieve sea ice thickness from CP data, simulated from the RADARSAT FP mode. They introduced a parameter, called CP ratio, which was found to be exponentially correlated with the sea ice thickness in addition to the dielectric constant of sea ice, ice surface roughness, and radar incidence angle. The parameter is defined in terms of element of the coherency matrix. Understandably, only level ice was considered in the study. Fig. 6 shows that negative trend of the CP ratio to the ice thickness, with higher sensitivity, as expected, in the thin ice range up to, say, 40 cm. The relation extends to 2.2 m ice thickness is an interesting and
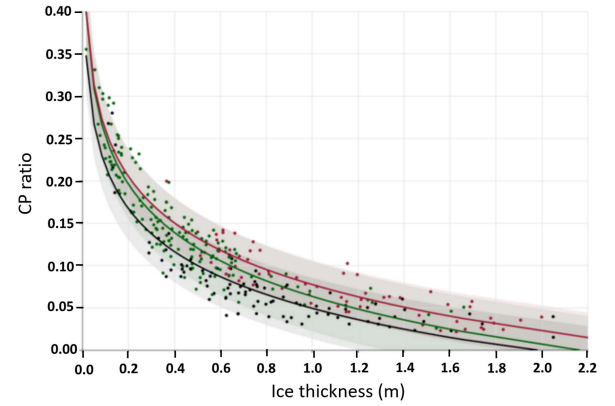

Fig. 6. Exponential regression relating sea ice thickness to the CP ratio. The black, green, and red lines are exponential fits for incidence angles 29°, 42°, and 49°. Shaded areas represent the 90% confidence intervals (adapted from [83]).

promising aspect though it needs sensitivity analysis, physical interpretation, and a proof of robustness of application.

VIII. OPERATIONAL USE OF POLARIMETRIC SAR IN SEA ICE MONITORING

Operational use of SAR for sea ice type and surface feature mapping relies on visual analysis of imagery data as no digital method has been developed to fulfill the accuracy, robustness, and the short turnaround time needed for the operational environment. Operational sea ice monitoring is geared toward using a color scheme for interpretation of CP data, now available from the RCM system. First attempts of using polarimetric SAR data in visual image schemes to map sea ice have been developed recently. A color composite with RGB representing three CP parameters: CPSeaIce$_{\text{Depol}}$, CPSeaIce$_{\text{Delta}}$, and CPSeaIce$_{\text{Rco}}$, respectively, was developed in [37]. The first parameter emphasizes sea ice types that have multiple surface scattering and/or a strong volume scattering (e.g., MYI). The second emphasizes sea ice types that exhibit phase difference between RV and RH scattering (e.g., thin ice). The third emphasizes ice types that exhibit polarization diversity such as early-stage types (including FYI) and FYI with ponds. In [20] another color composite scheme, called Scat-SeaIce, was developed. It integrated three FP parameters from the PDP set: SPAN, P_v/P_s, and entropy in an RGB color scheme, respectively. An example of the SPAN image and the two schemes is shown Fig. 7. It is clear in the SPAN image that the scene encompasses mostly FYI (moderate grey tone), MYI (high grey tone at the right side), and thin/new ice (dark tone). Those ice types appear in reddish, pinkish, and blueish colors, respectively, in the Scat-SeaIce composite scheme. Less color variety appears in the CPSeaIce scheme.

In general, polarimetric SAR parameters (including power from scattering mechanisms) are triggered by several factors from snow-covered sea ice. Some of those factors became known through the numerous studies on backscatter from sea ice cover under different surface, age, and meteorological conditions. However, the factors affecting the polarimetric parameters (especially the PDPs) are still being explored in research studies. Both
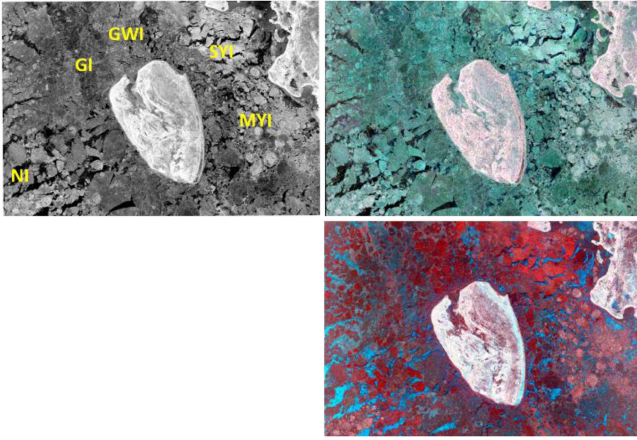
Fig. 7.   RADARSAT-2 FP scene of resolute bay acquired on 14 October 2017 (top left), the color composite scheme CPSeaIce is shown in the top right panel and the color composite scheme Scat-SeaIce is shown in the bottom right panel. NI, GI, GWI, SYI, and MYI stand for new ice, grey ice, grey-white ice, second-year ice, and multiyear ice, respectively. Ice types are identified in the CIS ice daily ice charts.
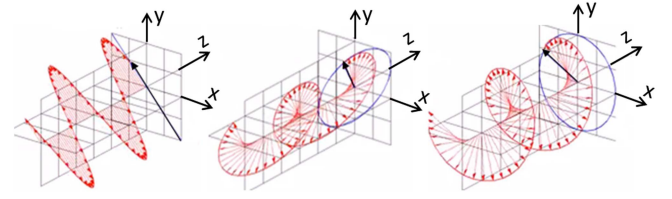

Fig. 8.   Propagation of the electric field in an EM wave in linearly-polarized pattern (left), elliptically polarized pattern (middle) and circularly polarized pattern (right).

research and operational use of polarimetric data will benefit from links established between those parameters and ice properties (including surface features). Those links can be identified using coincident data from satellite/airborne FP or CP systems or a ground-based scatterometer system as demonstrated in [84].

However, even if more useful links are established and proved to enhance the operational sea ice mapping, it seems that ancillary data will continue to be indispensable during the SAR image interpretation for resolving ambiguities and achieving the required operational accuracy and robustness.

IX. CONCLUSION

Polarimetric SAR observations available from FP or CP systems offer parameters which fully describe the polarization characteristics of the scattered signal from the observed surface. In addition, these extra observations still include the intensity and phase of the scattered signal as well as the power from the three scattering mechanisms; single-, double-, and multiple-bounce. Those parameters can be utilized to retrieve more accurate and robust information about snow-covered sea ice. Research for using polarimetric parameters in retrieving sea ice and snow information has been motivated by the operational use of those parameters to improve the operational sea ice monitoring. There is potential for switching to CP data for this purpose but this depends on proper training of ice analysts on visual interpretation of the CP parameters. This review introduces a brief theoretical background of the FP and CP SAR systems with their key derived parameters, and highlights their uses in retrieving conventional sea ice information such as ice types and thickness as well as new retrievals such as identification of new ice, ice ridging/rafting and discrimination between hummock and depression surfaces of MYI. A focus is placed on using the power from radar scattering mechanisms to retrieve new information, which cannot be retrieved from conventional SAR backscatter data. More potential applications are yet to evolve as the data

from the operational spaceborne CP mode are being evaluated and tested. To support this potential, it is recommended to acquire coincident *in situ* measurements of snow and ice physical properties and link them to the new polarimetric parameters.

APPENDIX

A. Polarization of Radar Signal

SAR transmits polarized pulses, which means that as the electromagnetic (EM) wave propagates the electric field has a predictable alignment. The alignment is defined according to the track of the tip of the electric field of the wave when projected on a plane perpendicular to the direction of the wave propagation (see Fig. 8). There are three categories of the predicted pattern of the wave propagation: linear, elliptic, and circular. In the linearly polarized EM wave, the propagation continues in the same plane, hence traces a line in the perpendicular plane. While the line can be at any angle, it is always at 0° (horizontal) or 90° (vertical) in the current operational SAR systems. In the elliptically polarized and circularly polarized EM, the path traces an ellipse and a circle, respectively. The linearly- and circularly polarized waves are special cases of the elliptically polarized wave. The EM wave can be fully polarized, partially polarized, or unpolarized. In classical literature, the polarization state of the EM wave is expressed by a vector known as Stokes vector [85]. The degree of polarization can be derived from this vector.

B. Formulation of Parameters Derived From FP SAR Observations

The scattering matrix $[S]$ is the elementary observation of the SAR FP mode at each pixel. It is an array of four complex elements that describe the transformation of the polarization of an incident wave pulse E^i on a reflective medium to the polarization of the backscattered wave E^s [17]

$$\left[\begin{array}{c} E_h^s \\ E_v^s \end{array} \right] = [S] \left[\begin{array}{c} E_h^i \\ E_v^i \end{array} \right] = \left[\begin{array}{cc} S_{hh} & S_{hv} \\ S_{vh} & S_{vv} \end{array} \right] \left[\begin{array}{c} E_h^i \\ E_v^i \end{array} \right] \quad (B-1)$$

where E is the electric field intensity, superscripts i and s denote the transmitted and the scattered signal, respectively, and subscripts h and v refer to horizontal and vertical linear polarizations, respectively. Elements of this matrix are complex quantities, which combine the intensity and the phase of the recorded signal.

Two sets of parameters can be derived to describe the polarimetric behavior of the ground cover, i.e., a noncoherent

surface. The first, which is referred to as polarimetric ratios and coherence (PRC), is derived directly from elements of the scattering matrix. The second, known as polarimetric decomposition parameters (PDP) is derived from second-order matrices, obtained from vectors composed of elements of the scattering matrix. The PDPs are indirect or direct expressions of the power from the scattering mechanisms (see Section II). If associated with a dominant mechanism, a ground cover can be uniquely identified using parameters from this set.

1) PRC Parameters: The PRC set includes the total power ($SPAN$), the copolarization and cross-polarization ratios ($R_{hh/vv}$, $R_{hh/hv}$, and $R_{vv/hv}$), the depolarization correlation coefficient R_{depol} (this is the ratio of the cross-pol to multiplication of both co-pol channels), the copolarization phase difference ϕ_{hh-vv}, and the copolarization correlation coefficient r_{hh-vv}. Mathematical expressions are as follows:

$$\text{SPAN} = \langle S_{hh}S_{hh}^* \rangle + \langle S_{vv}S_{vv}^* \rangle + 2\langle S_{hv}S_{hv}^* \rangle \quad (B-2)$$

$$R_{hh/vv} = \frac{\langle S_{hh}S_{hh}^* \rangle}{\langle S_{vv}S_{vv}^* \rangle} \quad (B-3)$$

$$R_{hh/hv} = \frac{\langle S_{hh}S_{hh}^* \rangle}{\langle S_{hv}S_{hv}^* \rangle} \quad (B-4)$$

$$R_{\text{depol}} = \frac{\langle S_{vh}S_{hv}^* \rangle}{\sqrt{\langle S_{vv}S_{vv}^* \rangle \langle S_{hh}S_{hh}^* \rangle}} \quad (B-5)$$

$$\phi_{hh-vv} = \tan^{-1}\left[\frac{\text{Im}\langle S_{hh}S_{vv}^* \rangle}{\text{Re}\langle S_{hh}S_{vv}^* \rangle}\right] \quad (B-6)$$

$$r_{hh-vv} = \left|\frac{\langle S_{hh}S_{vv}^* \rangle}{\sqrt{\langle S_{hh}S_{hh}^* \rangle \langle S_{vv}S_{vv}^* \rangle}}\right| \quad (B-7)$$

where Re and Im are the real and imaginary components of the complex number, $\langle \blacksquare \rangle$ denotes the ensemble average over a few of neighboring pixels, $*$ denotes complex conjugate, and $|\blacksquare|$ is modulus of complex number. High cross-polarization ratio and the depolarization correlation coefficients are indicators of the multiple (random) scattering mechanism, which depolarizes the scattered signal. ϕ_{hh-vv} around 180° indicates ideal odd-bounce scattering from a smooth surface, while 0° indicates ideal double-bounce scattering from a dihedral-like landscape structure.

2) PDP Parameters: The PDPs are obtained from decomposition of matrices derived from the scattering matrix. Three decomposition methods are presented in the following and have been used in sea ice applications. The first is derived from the eigen decomposition of the coherency matric (B-11), which is a purely mathematical-based decomposition, known as Cloude–Pottier decomposition. It provides proxy indicators of the relative power of the three scattering mechanisms. The second is model-based decomposition such as the Yamaguchi decomposition, which is based on the covariance matrix decomposition. This decomposition offers the absolute power of each scattering mechanism within the total power (SPAN). The third, known as Touzi decomposition, is based on a scattering vector model for the representation of coherent target scattering based on the projection of the Kennaugh–Huynen scattering matrix

con-diagonalization into the Pauli basis. Details are given as follows.

The coherency and covariance matrices are second-order statistics based on vectorization of the scattering matrix. Two scattering vectors can be derived from $[S]$, the lexicological and the Pauli [16]. Assuming the reciprocity condition which implies $S_{hv} = S_{vh}$, the lexicological scattering vector can take the form

$$\text{K}_{\text{L}} = [S_{hh}, \ S_{vv}, \ 2S_{hv}]^T \quad (B-8)$$

where the superscript T denotes the vector transpose. An ensemble average of the complex product of the lexicological scattering vector K_{L} with its complex conjugate transpose K_{L}^{*T} leads to a second-order matrix known as polarimetric covariance matrix [C]. This is a second-order matrix that takes the following form [16]:

$$[\text{C}] = \langle \text{K}_{\text{L}}.\text{K}_{\text{L}}^{*T} \rangle. \quad (B-9)$$

On the other hand, the Pauli vector K_{P} is defined as follows:

$$\text{K}_{\text{P}} = \frac{1}{\sqrt{2}}[(S_{hh} + S_{vv}), \ (S_{hh} - S_{vv}), \ 2\,S_{hv}]^T. \quad (B-10)$$

An ensemble average of the complex product of K_{p} with its complex conjugate transpose K_{p}^{*T} leads to another second-order matrix called polarimetric coherency matrix [T], which takes the form

$$[\text{T}] = \langle \text{K}_{\text{p}}\text{K}_{\text{p}}^{*T} \rangle. \quad (B-11)$$

The sum of the diagonal elements of [C] or [T] represents the *SPAN* parameter. The eigen decomposition of [T], known as Cloude–Pottier decomposition [25], takes the form

$$[\text{T}] = [\text{U}][\Lambda][\text{U}]^{*T} = [\text{U}]\begin{bmatrix} \lambda_1 & 0 & 0 \\ 0 & \lambda_2 & 0 \\ 0 & 0 & \lambda_3 \end{bmatrix}[\text{U}]^{*T} \quad (B-12)$$

where $\lambda_1 \geq \lambda_2 \geq \lambda_3 \geq 0$ are the real eigenvalues and $[\text{U}]$ is the unitary matrix, whose columns correspond to the orthogonal eigenvectors of $[\text{T}]$. Three PDPs can be derived from the eigenvalues; the entropy (H), anisotropy (A), and alpha-angle (α)

$$H = -\sum_{i=1}^{3} \text{P}_i \log_3 \text{P}_i \quad (B-13)$$

where $\text{P}_i = \lambda_i / \sum_{i=1}^{3} \lambda_i$.

$$A = \frac{\lambda_2 - \lambda_3}{\lambda_2 + \lambda_3} \quad (B-14)$$

$$\alpha = \sum_{i=1}^{3} \text{P}_i \alpha_i. \quad (B-15)$$

The entropy $(0 \leq H \leq 1)$ is an indicator of the number of effective scattering mechanisms in the observed backscatter. When H is low, only one deterministic mechanism is expected, either SB or DB. High values of H indicate strong random scattering (i.e., MB mechanism). For medium values of H, A should be examined (since $\lambda_2 > \lambda_3$, then $0 \leq A \leq 1$). Low values

of A mean two comparable secondary mechanisms and high values mean one significant secondary mechanism. Note that if both λ_2 and λ_3 are very small, the resulting anisotropy can be just noise. The values of α fall between $0°$ and $90°$. Value close to zero indicate domination of the SB scattering while values close to $90°$ indicate significant DB scattering mechanism. Values between $40°$ and $50°$ indicate dipole MB (random) scattering mechanism. If H is very low, α is needed to determine whether the dominant mechanism is SB or DB. All of the PDPs offer information on the relative (not absolute) power from the three scattering mechanisms. They are indicators of the number, the type(s), and relative weight of the scattering mechanisms.

The absolute power of each scattering mechanism can be revealed using model-based decomposition methods, such as the Yamaguchi decomposition parameters [86]. This is a four-component model-based polarimetric decomposition, which is an extension of the three-component Freeman–Durden decomposition [87]. It is based on modeling the covariance matrix $[C]$ into four scattering matrices corresponding to surface (single) scattering, double-bounce scattering, multiple (random or volume) scattering, and helix scattering mechanisms. The powers are denoted by the four subscripts s, d, v, and c, respectively, as shown in the following equation:

$$[C] = f_s[C]_s + f_d[C]_d + f_v[C]_v + f_c[C]_c \quad (B-16)$$

where f is the weight (coefficient) of the relevant mechanism. Only the first three components are used for sea ice applications. The last one is more suitable for urban applications. The power derived from the coefficients are denoted P_s, P_d, and P_v (surface, double, and volume, respectively). The ratio P_v/P_s is used in this review as an indicator that identifies ice types/surfaces which return comparable volume and surface scattering.

In its incoherent form, Touzi decomposition [88] allows for the representation of the coherency matrix as the incoherent sum of three coherency matrices $[T]_i$ ($i = 12,3$) representing three different single scatterers, weighted by its positive real eigenvalue $[\eta_i]$

$$[T] = \sum_{i=12,3} \eta_i[T]_i. \quad (B-17)$$

Four unique roll-invariant target parameters can be derived from the Touzi decomposition. They describe the target orientation angle (ψ_i), the target helicity (τ_{m_i}), the scattering type magnitude (α_{s_i}), and the scattering type phase (ϕ_{s_i})

$$\alpha_s = \sum_{i=12,3} \lambda_i \alpha_{s_i} \quad (B-18)$$

$$\phi_s = \sum_{i=12,3} \lambda_i \phi_{s_i} \quad (B-19)$$

$$\psi = \sum_{i=12,3} \lambda_i \psi_i, \quad (B-20)$$

$$\tau_m = \sum_{i=12,3} \lambda_i \tau_{m_i} \quad (B-21)$$

where $\lambda_i = {\eta_i}/{(\eta_1 + \eta_2 + \eta_3)}$.

TABLE I
COMPACT POLARIMETRIC (CP) PARAMETERS

Short form	Description
$\sigma^0_{RH}, \sigma^0_{RV},$ $\sigma^0_{RL}, \sigma^0_{RR}$	Sigma naught backscattering—right circular transmit and horizontal linear, vertical linear, left circular, or right circular receive polarization [13]
m-χ_S, m-χ_V, m-χ_DB	surface, volume, double bounce scattering from m-χ decomposition [90]
m-δ_S, m-δ_V, m-δ_DB	surface, volume, double bounce and scattering from m-δ decomposition [7]
SV0, SV1, SV2, SV3	Stokes vector elements [87]
SE_Pol, SE_Int	Shannon entropy polarimetric and intensity components [91]
M	Degree of polarization [26]
M	Conformity coefficient [92]
ρ_{RHRV}	RH RV correlation coefficient [13]
$\sigma^0_{RR}/\sigma^0_{RL}$	Circular polarization ratio
α_s	Alpha feature related to the ellipticity of the compact scattered wave [85]
δ_{RHRV}	RH RV phase difference [8]

The α_s parameter represents the magnitude of the symmetric scattering type and varies within the interval [0, 90°]. The ϕ_s parameter, ranging between [−90°, 90°] represents the phase of the symmetric scattering type. It is equal to the phase difference between HH and VV but only for very low HV component. The ψ parameter ranging between [−90°, 90°] determines the target orientation angle about the radar line of sight. The helicity τ_m is used for identifying the symmetric nature of the radar target and varies between −45° and 45°.

C. Formation of Parameters Derived From CP SAR Observations

Assuming a transmitting right circular signal (R) and coherently receiving linear (horizontal and vertical) signals, the complex CP products S_{RH} and S_{RV} can be given as follows:

$$S_{RH} = \frac{1}{\sqrt{2}}(S_{HH} - iS_{HV}) \quad (C-1)$$

$$S_{RV} = \frac{1}{\sqrt{2}}(S_{VH} - iS_{VV}). \quad (C-2)$$

The complex RH and RV scattering elements are converted to Stokes vector, which can then be speckle filtered and used for the extraction of the CP parameters shown in Table B2. Detailed information about calculations of these parameters is presented in [13]. It should be noted that aspects of target decomposition

theory for use with CP radar data were developed in [89] by making link between fully FP and CP systems. The authors showed that, under certain assumptions, CP data can be used to estimate the rotation invariant alpha angle of FP systems, which can then be used for polarimetric classification and physical parameter estimation.

ACKNOWLEDGMENT

REFERENCES

[1] M. Shokr, "Towards a better utilization of SAR data in sea ice monitoring," in *Proc. 1st Workshop ERS-1 Pilot Projects*, 1994, pp. 163–168.

[2] S. Sandven, O. M. Johannessen, M. W. Miles, L. H. Pettersson, and K. Kloster, "Barents sea seasonal ice zone features and processes from ERS 1 synthetic aperture radar: Seasonal ice zone experiment 1992," *J. Geophys. Res.*, vol. 104, no. C7, pp. 15843–15857, 1999.

[3] M. Mäkynen and M. Hallikainen, "Investigation of C-band and X-band backscattering signatures of the baltic sea ice," *Int. J. Remote Sens.*, vol. 25, no. 11, pp. 2061–2086, 2004.

[4] S. Sandven, V. Alexandrov, N. Zakhvatkina, and M. Babiker, "Sea ice classification using RADARSAT-2 dual polarisation data," in *Proc. 4th Int. Workshop Adv. SAR Oceanogr.*, 2012, pp. 1–10.

[5] M. Shokr, B. Ramsay, and J. C. Falkingham, "Operational use of ERS-1 SAR images in the Canadian ice monitoring program," *Int. J. Remote Sens.*, vol. 17, no. 4, pp. 667–682, 1996.

[6] J. J. van der Sanden, "Anticipated potential of radarsat-2 data," *Can. J. Remote Sens.*, vol. 30, no. 3, pp. 369–379, 2004.

[7] R. K. Raney, "Hybrid-polarity SAR architecture," *IEEE Trans. Geosci. Remote Sens.*, vol. 45, no. 11, pp. 3397–3404, Nov. 2007.

[8] F. Charbonneau et al., "Compact polarimetry overview and applications assessment," *Can. J. Remote Sens.*, vol. 36, pp. 298–315, 2010.

[9] H. Bouzerar, S. Mebrek, B. Souissi, and A. Daamouche, "Compact and full polarimetric SAR imaging for target characterization," in *Proc. Mediterranean Middle-East Geosci. Remote Sens. Symp.*, 2020, pp. 61–64, doi: 10.1109/M2GARSS47143.2020.9105325.

[10] R. Touzi, "Compact-hybrid versus linear dual and fully polarimetric SAR," in *Proc. 4th Int. Workshop Sci. Appl. SAR Polarimetry Polarimetric Interferometry*, 2009, pp. 1–22.

[11] M. M. Espeseth, C. Brekke, and A. M. Johansson, "Assessment of RISAT-1 and radarsat-2 for sea ice observations from a hybrid-polarity perspective," *Remote Sens.*, vol. 9, no. 11, 2017, Art. no. 1088, doi: 10.3390/rs9111088.

[12] B. Brisco, M. Mahdianpari, and F. Mohammadimanesh, "Hybrid compact polarimetric SAR for environmental monitoring with the RADARSAT constellation mission," *Remote Sens.*, vol. 12, 2020, Art. no. 3283, doi: 10.3390/rs12203283.

[13] M. Dabboor and T. Geldsetzer, "Towards sea ice classification using simulated RADARSAT constellation mission compact polarimetric SAR imagery," *Remote Sens. Environ.*, vol. 140, pp. 189–195, 2014, doi: 10.1016/j.rse.2013.08.035.

[14] M. R. Drinkwater, R. Kwok, E. Rignot, H. Israelsson, R. G. Onstott, and D. P. Winebrenner, "Potential applications of polarimetry to the classification of sea ice," in *Microwave Remote Sensing of Sea Ice*, F. Carsey, Ed. Washington, DC, USA: Amer. Geophys. Union, 1992.

[15] W. Dierking, "Sea ice monitoring by synthetic aperture radar," *Oceanography*, vol. 26, no. 2, pp. 100–111, 2013, doi: 10.5670/oceanog.2013.33.

[16] N. Zakhvatkina, V. Smirnov, and I. Bychkova, "Satellite SAR data-based sea ice classification: An overview," *Geosciences*, vol. 9, no. 4, 2019, Art. no. 152, doi: 10.3390/geosciences9040152.

[17] J. Lee and E. Pottier, *Polarimetric Radar Images: From Basic to Applications*. Boca Raton, FL, USA: CRC Press, 2009, p. 422.

[18] J. J. Van Zyl and Y. Kim, *Synthetic Aperture Radar Polarimetry*. Hoboken, NJ, USA: Wiley, 2011, p. 312.

[19] C. López-Martínez and E. Pottier, "Basic principles of SAR polarimetry," in *Polarimetric Synthetic Aperture Radar: Principles and Applications* (Remote Sensing and Digital Image Processing Book Series), vol. 25. I. Hajnsek and Y.-L. Desnos, Eds. Berlin, Germany: Springer, 2021, ch. 1, pp. 1–58.

[20] M. Shokr, M. Dabboor, M. Lacelle, T. Zagon, and B. Deschamps, "Observations from C-band SAR fully-polarimetric parameters of mobile sea ice based on radar scattering mechanisms to support operational sea ice monitoring," *Can. J. Remote Sens.*, vol. 48, no. 2, pp. 197–213, 2022.

[21] P. H. LeBlond and L. A. Mysak, "Waves in the ocean," in *Elsevier Oceanography Series*. Amsterdam, The Netherlands: Elsevier, 1981.

[22] S. G. Beaven, "Sea ice radar backscatter modeling, measurements and the fusion of active and passive microwave data," Radar Syst. Remote Syst. Lab., Dept. Elect. Eng. Comput. Sci., Univ. Kansas, Lawrence, KS, USA, Tech Rep. 8243-4, 1991.

[23] M. Shokr and N. K. Sinha, "Arctic sea ice microstructure observations relevant to microwave scattering," *Arctic*, vol. 47, no. 3, pp. 265–279, 1994.

[24] M. Dabboor, B. Montpetit, S. E. L. Howell, and C. Haas, "Improving sea ice characterization in dry ice winter conditions using polarimetric parameters from C- and L-band SAR data," *Remote Sens.*, vol. 9, 2017, Art. no. 1270.

[25] S. R. Cloude and E. Pottier, "An entropy-based classification scheme for land applications of polarimetric SAR," *IEEE Trans. Geosci. Remote Sens.*, vol. 35, no. 1, pp. 68–78, Jan. 1997.

[26] M. Dabboor and M. Shokr, "Compact polarimetry response to modeled fast sea ice thickness," *Remote Sens.*, vol. 12, 2020, Art. no. 3240, doi: 10.3390/rs12193240.

[27] S. V. Nghiem, R. Kwok, S. H. Yueh, and M. R. Drinkwater, "Polarimetric signatures of sea ice part 2. Experimental observations," *J. Geophys. Res.*, vol. 100, no. C7, pp. 13681–13698, 1995a.

[28] H. Wakabayashi, T. Matsuoka, K. Nakamura, and F. Nishio, "Polarimetric characteristics of sea ice in the sea of Okhotsk observed by airborne L-band SAR," *IEEE Trans. Geosci. Remote Sens.*, vol. 42, no. 11, pp. 2412–2425, Nov. 2004.

[29] T. Geldsetzer and J. J. Yackel, "Sea ice type and open water discrimination using dual co-polarized C-band SAR," *Can. J. Remote Sens.*, vol. 35, no. 1, pp. 73–84, 2009.

[30] J. P. S. Gill and J. J. Yackel, "Evaluation of C-band SAR polarimetric parameters for discrimination of first-year sea ice types," *Can. J. Remote Sens.*, vol. 38, no. 3, pp. 306–323, 2012.

[31] J. P. S. Gill, J. J. Yackel, T. Geldsetzer, and M. C. Fuller, "Sensitivity of C-band synthetic aperture radar polarimetric parameters to snow thickness over landfast smooth first-year sea ice," *Remote Sens. Environ.*, vol. 166, pp. 34–49, 2015, doi: 10.1016/j.rse.2015.06.005.

[32] M. Shokr and M. Dabboor, "Observations of SAR polarimetric parameters of lake and fast sea ice during the early growth phase," *Remote Sens. Environ.*, vol. 247, 2020, Art. no. 111910.

[33] D. Isleifson, B. Hwang, D. G. Barber, R. K. Scharien, and L. Shafai, "C-band polarimetric backscattering signatures of newly formed sea ice during fall freeze-up," *IEEE Trans. Geosci. Remote Sens.*, vol. 48, no. 1, pp. 3256–3267, Aug. 2010.

[34] A. M. Johansson, C. Brekke, G. Spreen, and J. A. King, "X-, C-, and L-band SAR signatures of newly formed sea ice in Arctic leads during winter and spring," *Remote Sens. Environ.*, vol. 204, pp. 162–180, 2017.

[35] M. Shokr and N. K. Sinha, *Sea Ice: Physics and Remote Sensing*, 2nd ed. Hoboken NJ, USA: Wiley, 2023.

[36] M. Dabboor, B. Montpetit, and S. E. L. Howell, "Assessment of the high-resolution SAR mode of the RADARSAT constellation mission for first year ice and multiyear ice characterization," *Remote Sens.*, vol. 10, no. 4, 2018, Art. no. 594, doi: 10.3390/rs10040594.

[37] T. Geldsetzer, M. Arkett, T. Zagon, F. Charbonneau, J. Tackel, and R. K. Scharien, "All-season compact-polarimetry C-band SAR observations of sea ice," *Can. J. Remote Sens.*, vol. 41, no. 5, pp. 485–504, 2015.

[38] S. Singha and R. Ressel, "Arctic sea ice characterization using RISAT-1 compact-pol SAR imagery and feature evaluation: A case study over Northeast Greenland," *IEEE J. Sel. Topics Appl. Earth Observ. Remote Sens.*, vol. 10, no. 8, pp. 3504–3514, Aug. 2017.

[39] M. Dabboor and M. Shokr, "Investigation of the sensitivity response of Touzi target scattering decomposition to modeled early ice growth," *Int. J. Remote Sens.*, vol. 44, no. 11, pp. 3456–3473, 2023.

[40] F. A. Zebker and J. J. van Zyl, "Imaging radar polarimetry: A review," *Proc. IEEE*, vol. 79, no. 11, pp. 1583–1606, Nov. 1991.

[41] W. Dieking, H. Skriver, and P. Gudmandsen, "SAR polarimetry for sea ice classification," in *Proc. Workshop POLinSAR: Appl. SAR Polarimetry Polarimetric Interferometry*, 2003, pp. 14–16.

[42] R. Horn, R. Scheiber, J. Amao-Oliva, R. Haensch, F. Weinmann, and M. Jaeger, "ICESAR 2019: A study on sea ice based on F-SAR X-, C-, L-band data," in *Proc. 13th Eur. Conf. Synthetic Aperture Radar*, 2021, Art. no. 104.

[43] MANICE, Manual of Standard Procedures for Observing and Reporting Ice Conditions, Canadian Ice Service – Environment Canada, Toronto, ON, Canada, Catalogue No. EN56-175/2005, 2005.

[44] A. Gegiuc, M. Similä, J. Karvonen, M. Lensu, M. Mäkynen, and J. Vainio, "Estimation of degree of sea ice ridging based on dual-polarized C-band SAR data," *Cryosphere*, vol. 12, pp. 343–364, 2018, doi: 10.5194/tc-12-343-2018.

[45] L.-K. Soh, C. Tsatsoulis, D. Gineris, and C. Bertoia, "ARKTOS: An intelligent system for SAR sea ice image classification," *IEEE Trans. Geosci. Remote Sens.*, vol. 42, no. 1, pp. 229–248, Jan. 2004.

[46] Y. Hara, R. G. Atkins, R. T. Shin, J. K. Kong, S. H. Yueh, and R. Kwok, "Application of neural networks for sea ice classification in polarimetric SAR images," *IEEE Trans. Geosci. Remote Sens.*, vol. 33, no. 3, pp. 740–748, May 1995.

[47] B. Scheuchi, R. Caves, I. Cumming, and G. Staples, "Authomated sea ice classification using spaceborne polarimetric SAR data," in *Proc. Scanning Present Resolving Future. IEEE Int. Geosci. Remote Sens. Symp.*, 2001, vol. 7, pp. 3117–3119.

[48] B. Scheuchl, I. G. Cumming, and I. Hajnsek, "Classification of fully polarimetric single- and dual-frequency SAR data of sea ice using the wishart statistics," *Can. J. Remote Sens.*, vol. 31, pp. 61–72, 2005.

[49] A. Marino, W. Dierking, I. Hajnsel, and C. Wesche, "SAR polarimetry for classification of sea ice: A comparison of physical based algorithms on ICESAR data," in *Proc. ESA Living Planet Symp.*, 2013, Art. no. 34766.

[50] C. Brekke, B. Holt, C. Jones, and S. Skrunes, "Discrimination of oil spills from newly formed sea ice by synthetic aperture radar," *Remote Sens. Environ.*, vol. 145, pp. 1–14, 2014, doi: 10.1016/j.rse.2014.01.015.

[51] M. Dabboor and M. Shokr, "A new Bayesian likelihood ratio test for supervised classification of fully polarimetric SAR data: An application for sea ice type mapping," *ISPRS J. Photogrammetry Remote Sens.*, vol. 84, pp. 1–11, 2013.

[52] M.-A. N. Moen, S. N. Anfinsen, A. P. Doulgeris, A. H. H. Renner, and S. Gerland, "Assessing polarimetric SAR sea-ice classifications using consecutive day images," *Ann. Glaciol.*, vol. 56, no. 69, pp. 285–294, 2015.

[53] R. Ressel, S. Singha, S. Lehner, A. Rosel, and G. Spreen, "Investigation into different polarimetric features for sea ice classification using X-band synthetic aperture radar," *IEEE J. Sel. Topics Appl. Earth Observ. Remote Sens.*, vol. 9, no. 7, pp. 3131–3143, Jul. 2016.

[54] Q. Zhao, S. Guo, X. Li, and Y. Li, "Polarimetric SAR sea ice classification based on target decompositional features," *Acta Geodaetica et Cartographica Sin.*, vol. 47, no. 12, pp. 1609–1629, 2018.

[55] S. Singha, M. Johansson, N. Hughes, S. M. Hvidegaard, and H. Skourup, "Arctic sea ice characterization using spaceborne fully polarimetric L-, C-, and X-band SAR with validation by airborne measurements," *IEEE Trans. Geosci. Remote Sens.*, vol. 56, no. 7, pp. 3715–3734, Jul. 2018.

[56] T. Zhang et al., "Deep learning based sea ice classification with GAOFFEN-3 fully polarimetric SAR data," *Remote Sens.*, vol. 13, no. 8, 2021, Art. no. 1452, doi: 10.3390/RS13081452.

[57] B. Scheuchi, I. Hajnsek, and I. G. Cumming, "Sea ice classification using multi-frequency polarimetric SAR data," in *Proc. Geosci. Remote Sens. Symp.*, 2002, vol. 3, pp. 1914–1916, doi: 10.1109/IGARSS.2002.1026298.

[58] B. Scheuchi, I. Hajnsek, and I. G. Cumming, "Model-based classification of polarimetric SAR sea ice data," in *Proc. Geosci. Remote Sens. Symp.*, 2002, vol. 3, pp. 1521–1523, doi: 10.1109/IGARSS.2002.1026168.

[59] W. Dierking et al., "Sea ice deformation mapping by means of SAR," in *Proc. Eur. Conf. Synthetic Aperture Radar*, 2006, pp. 1–4.

[60] S. S. Cafarella et al., "Estimation of level and deformed first-year ice surface roughness in the Canadian arctic archipelago from C- and L-band synthetic aperture radar," *Can. J. Remote Sens.*, vol. 45, no. 8, pp. 1–19, 2019.

[61] R. A. Segal, R. K. Scharien, S. Cafarell, and A. Tesstone, "Characterizing winter landfast sea-ice surface roughness in the Canadian arctic archipelago using sentinel-1 synthertic aperture radar and multi-angle imaging spectroradiometer," *Ann. Glaciol.*, vol. 61, no. 83, pp. 284–198, 2020.

[62] Z. Chen et al., "Insar monitoring of Arctic land fast sea ice deformation using L-band ALOS-2, C-band RADARSAT-2 and sentinel-1," *Remote Sens.*, vol. 13, no. 22, 2021, Art. no. 4570, doi: 10.3390/rs13224570.

[63] D. O. Dammann, H. Eicken, A. R. Mahoney, E. Saiet, F. J. Meyer, and J. C. George, "Traversing sea ice-linking surface roughness and ice trafficability through SAR polarimetry and interferometry," *IEEE J. Sel. Topics Appl. Earth Observ. Remote Sens.*, vol. 11, no. 2, pp. 416–433, Feb. 2018.

[64] H. Han et al., "Surface roughness signature of summer Arctic snow-covered sea ice in X-band dual-polarimetric SAR," *GIS Sci. Remote Sens.*, vol. 57, no. 5, pp. 650–669, 2020.

[65] E. Bailey, D. L. Feltham, and P. R. Sammonds, "A model for the consolidation of rafted sea ice," *J. Geophys. Res.*, vol. 115, 2010, Art. no. C004015, doi: 10.1029/2008JC005103.

[66] D.-J. Kim, B. Hwang, K. H. Chung, S. H. Lee, H.-S. Jung, and W. M. Moon, "Melt pond mapping with high resolution SA: The first view," *Proc. IEEE*, vol. 101, no. 3, pp. 748–758, Mar. 2013.

[67] S. Ramjan, T. Gelsetzer, R. K. Scharien, and J. J. Yackel, "Predicting melt pond fraction on landfast covered first year sea ice from winter C-band SAR backscattering utilizing linear, polarimetric and texture parameters," *Remote Sens.*, vol. 10, 2018, Art. no. 1603, doi: 10.3390/rs10101603.

[68] R. K. Scharien, J. J. Yackel, D. G. Barber, M. Asplin, M. Gupta, and D. Isleifson, "Geophysical controls on C-band polarimetric backscatter from melt pond covered Arctic first-year sea ice: Assessment using high-resolution scatterometry," *J. Geophysical Res. Ocean*, vol. 117, 2012, Art. no. C00G18, doi: 10.1029/2011JC007353.

[69] H. Han, I. J. Kim, S. Sim, J. Kim, D. J. Kim, and S. H. Kang, "Retrieval of melt pong on multiyear sea ice in summer from TerraSAR-X dual polarization data using machine learning approaches: A case study in the Chukchi Sea with mid-incidence angle data," *Remote Sens.*, vol. 8, no. 1, 2016, Art. no. 57, doi: 10.3390/rs8010057.

[70] A. S. Fors, D. V. Divine, A. P. Doulgeris, A. H. H. Renner, and S. Gerald, "Signature of arctic sea ice melt pond fraction in X-band SAR imagery," *Cryosphere*, vol. 11, pp. 755–771, 2017.

[71] H. Li, W. Perrie, Q. Li, and Y. Hou, "Estimation of melt pond fractions on first year sea ice using compact polarization SAR," *J. Geophys. Res. Oceans*, vol. 122, no. 10, pp. 8145–8166, 2017.

[72] T. C. Grenfell et al., "Considerations for microwave remote sensing of thin sea ice," in *Microwave Remote Sensing of Sea Ice*, F. Carsey, Ed. Washington, DC, USA: Amer. Geophys. Union, 1992.

[73] K. Nakamura, H. Wakabayashi, K. Naoki, F. Nishio, T. Moriyama, and S. Uratsuka, "Observation of sea-ice thickness in the sea of okhotsk by using dual-frequency and fully polarimetric airborne SAR (Pi-SAR) data," *IEEE Trans. Geosci. Remote Sens.*, vol. 43, no. 11, pp. 2460–2469, Nov. 2005.

[74] K. Nakamura, H. Wakabayashi, S. Uto, K. Naoki, F. Nishio, and S. Uratsuka, "Sea-ice thickness retrieval in the Sea of Okhotsk using dual-polarization SAR data," *Ann. Glaciol.*, vol. 44, pp. 261–268, 2006.

[75] J.-W. Kim, D.-J. Kim, and B. J. Hwang, "Characterization of Arctic sea ice thickness using high-resolution spaceborne polarimetric SAR data," *IEEE Trans. Geosci. Remote Sens.*, vol. 50, no. 1, pp. 13–22, Jan. 2012.

[76] W. Dierking, H. Skriver, and P. Gudmandsen, "On the improvement of sea ice classification by means of radar polarimetry," in *Proc. 23rd Symp. Eur. Assoc. Remote Sens. Lab.*, 2004, pp. 203–209.

[77] A. M. Johansson et al., "Combined observations of arctic sea ice with near-coincident co-located X-band, C-band, and L-band SAR satellite remote sensing and helicopter-borne measurements," *J. Geophys. Res. Oceans*, vol. 122, pp. 669–691, 2017, doi: 10.1002/2016JC012273.

[78] S. V. Nghiem, R. Kwok, S. H. Yueh, and M. R. Drinkwater, "Polarimetric signature of sea ice: Part 1: Theoretical model," *J. Geophys. Res.*, vol. 100, no. C7, pp. 13665–13679, 1995b.

[79] M. Hossain, J. J. Yackel, M. Dabboor, and M. C. Fuller, "Application of a three-component scattering model over snow-covered first-year sea ice using polarimetric C-band SAR data," *Int. J. Remote Sens.*, vol. 35, no. 5, pp. 1786–1803, 2014, doi: 10.1080/01431161.2013.879345.

[80] X. Zhang, W. Dierking, J. Zhang, and J. Meng, "A polarimetric decomposition method for ice in the Bohai sea using C-band PolSAR data," *IEEE J. Sel. Topics Appl. Earth Observ. Remote Sens.*, vol. 8, no, no. 1, pp. 47–66, Jan. 2015.

[81] M. Ghanbari, D. A. Clausi, L. Xu, and M. Jiang, "Contextual classification of sea ice types using compact polarimetric SAR data," *IEEE Trans. Geosci. Remote Sens.*, vol. 57, no. 10, pp. 7476–7491, Oct. 2019.

[82] X. Zhang, J. Zhang, M. Liu, and J. Meng, "Assessment of C-band compact polarimetry SAR for sea ice classification," *Acta Oceanologica Sin.*, vol. 35, pp. 79–88, 2016.

[83] X. Zhang, W. Dierking, J. Zhang, J. Meng, and H. Lang, "Retrieval of the thickness of undeformed sea ice from simulated C-band compact polarimetric SAR images," *Cryosphere*, vol. 10, pp. 1529–1545, 2016, doi: 10.5194/tc-10-1529.

[84] T. Geldsetzer, J. B. Mead, J. J. Yackel, R. K. Scharien, and S. E. L. Howell, "Surface-based polarimetric C-band scatterometer for field measurements of sea ice," *IEEE Trans. Geosci. Remote Sens.*, vol. 45, no. 11, pp. 3405–3416, Nov. 2007.

[85] S. R. Cloude, *Polarisation: Applications in Remote Sensing*. London, U.K.: Oxford Univ. Press, 2009.

[86] Y. Yamaguchi, T. Moriyama, M. Ishido, and H. Yamada, "Four-component scattering model for polarimetric SAR image decomposition," *IEEE Trans. Geosci. Remote Sens.*, vol. 43, no. 8, pp. 1699–1706, Aug. 2005.

[87] T. Freeman and S. L. Durden, "A three-component scattering model for polarimetric SAR data," *IEEE Trans. Geosci. Remote Sens.*, vol. 36, no. 3, pp. 963–973, May 1998.

[88] R. Touzi, "Target scattering decomposition in terms of roll invariant target parameters," *IEEE Trans. Geosci. Remote Sens.*, vol. 45, no. 1, pp. 73–84, Jan. 2007.

[89] S. R. Cloude, D. G. Goodenough, and H. Chen, "Compact decomposition theory," *IEEE Geosci. Remote Sens. Lett.*, vol. 9, no. 1, pp. 28–32, Jan. 2012.

[90] R. K. Raney, J. T. S. Cahill, G. W. Patterson, and D. B. J. Bussey, "The m-chi decomposition of hybrid dual-polarimetric radar data with application to lunar craters," *J. Geophysical Res.*, vol. 117, 2012, Art. no. E00H21, doi: 10.1029/2011IJE003986.

[91] R. Réfrégier, F. Goudail, P. Chavel, and A. Friberg, "Entropy of partially polarized light and application to statistical processing techniques," *J. Opt. Soc. Amer.*, vol. 21, pp. 2124–2134, 2004.

[92] M.-L. Truong-Loi, A. Freeman, P. C. Dubois-Fernandez, and E. Pottier, "Estimation of soil moisture and Faraday rotation from bare surfaces using compact polarimetry," *IEEE Trans. Geosci. Remote Sens.*, vol. 47, no. 11, pp. 3608–3615, Nov. 2009.

Mohammed Dabboor (Senior Member, IEEE) received the B.Sc. and M.Sc. degrees in geomatics engineering from the National Technical University of Athens, Athens, Greece, in 2003 and 2005, respectively, and the Ph.D. degree in spaceborne synthetic aperture radar remote sensing from the University of Calgary, Calgary, AB, Canada, in 2010.

He served as a Natural Sciences and Engineering Research Council of Canada (NSERC) Postdoctoral Visiting Fellow with the Science and Technology Branch, Environment and Climate Change Canada, Government of Canada, until February 2015. Following his postdoctoral studies, he worked as an interim Research Scientist with the NASA Marshall Space Flight Center, Huntsville, AL, USA, until August 2015. Since September 2015, he has been a Research Scientist with the Science and Technology Branch, Environment and Climate Change Canada, Government of Canada, Toronto, ON, Canada. His research focuses on the analyzing of fully and compact polarimetric SAR imagery, and spaceborne SAR mission design. Additionally, since 2021, he serves as a mission advisor in the European Space Agency's Mission Advisory Group (MAG) of the SEASTAR EE11 candidate mission.

Dr. Dabboor is an active member of various teams and working groups, including the Canadian Space Agency (CSA) User and Science Team of the RADARSAT Constellation Mission and the CSA Science Team for the calibration and validation of the SWOT satellite mission. He is also Canada's representative in the international Group on Earth Observations (GEO)—Climate Change working group. He was the recipient of several awards, including the Queen Elizabeth II Graduate Award, the Helmut Moritz Graduate Award, and the Canadian Geophysical Union Geodesy Section Best Student Paper Award in 2007.

Mohammed Shokr (Senior Member, IEEE) received the Ph.D. degree in aeronautical engineering from Cairo University, Giza, Egypt, in 1980.

Since 1982, he has been with Environment Canada, Toronto, ON, Canada, and he retired in 2020 as a scientist emeritus. In 1989, he started his research career on the remote sensing of sea ice to support the Canadian Ice Monitoring Program. He has participated in several field expeditions in the Arctic and the East coast of Canada to study sea ice physical properties in relation to its radiometric signature observed by passive and active microwave sensors. He was the Principal Investigator of several projects to develop algorithms of sea-ice parameter retrieval and evaluate the operational use of new remote sensing technologies for ice applications. Since 2016, he collaborated with Beijing Normal University and Wuhan University in China to support their research on polar sea ice. He coauthored a book titled *Sea Ice Physics and Remote Sensing* (Wiley). His research interests include microwave remote sensing sea ice and climate change impacts on polar ice.